

Edge Site Catalyzed Vanadyl Oxidation Elucidated by Operando Raman Spectroscopy

Hannes Radinger,^{*[a, b]} Felix Bauer,^[a] and Frieder Scheiba^[a]

The kinetic processes responsible for the efficient oxidation of dissolved vanadyl oxide species in the positive half-cell of a vanadium flow battery are far from being understood. Despite recent evidence that the reaction is most strongly favored at hydrogen-terminated graphite edge sites, a mechanism involving oxygen-containing surface groups has still been frequently reproduced to date. In this work, *operando* Raman spectroscopy follows the reaction at the interface between graphite-based model electrodes and vanadium-containing sulfuric acid as the electrolyte. The potential-dependent growth of different vibra-

tional modes is related to the electrocatalytic activity of the sample and allows to track the oxidation of the electrolyte species. Moreover, the results express vanadium reaction intermediates of dimeric origin only on the edge-exposed surface of graphite, which exhibits significantly higher electrochemical activity. No interaction with surface oxygen postulated before could be observed for the active electrodes at potentials relevant to the reaction. Instead, a new growing graphite-related feature shows direct electronic interactions between vanadium ions and carbon atoms during charge transfer.

Introduction

Contemporary electrochemistry seeks to use analytical tools that allow the dynamic examination of reaction processes on an electrode using *operando* techniques.^[1–3] The difficulty is to apply techniques that not only detect the bulk of a material but also allow monitoring of changes in the underlying surface structure, resulting reaction intermediates, or sorption processes. Raman spectroscopy is particularly suitable because it uses visible light, is applicable at elevated temperatures or pressures,^[3–5] and provides strong signals for typical catalytically active sites, such as molecular metal–oxygen vibrations^[6] or covalent carbon bonds. It therefore enjoys great popularity for many electrochemical systems and has been used to study the oxygen evolution reaction in metal oxides,^[7,8] lithiation^[9] and sodiation^[10] into carbon-based electrodes, or carbon dioxide reduction on copper.^[11,12]

In contrast, only one very recent study examined the reaction mechanism for the oxidation of $V^{IV}O^{2+}$ to $V^{V}O_2^+$ on carbon paper,^[13] which comprises the kinetic bottleneck in the positive half-cell of a vanadium flow battery.^[14] On highly

oxidized electrodes, the reaction was reported to proceed *via* the formation of vanadium dimers on oxygen functionalized surfaces, complementing the originally proposed reaction mechanism through C–O–V intermediates,^[15] which has been widely reproduced to date for a variety of carbon-based electrodes, such as fibers,^[16,17] paper,^[18] and graphene.^[19] However, our previous results paint a different picture, showing that hydrogen-terminated defects on the surface of graphite provide much faster and more reliable charge transfer kinetics for the vanadium redox reactions than oxygen-containing functional groups.^[20,21] The *operando* study mentioned above^[13] demonstrated the interaction of vanadium with surface oxygen species by analyzing a small wavenumber range with relatively low intensity between 700 to 1100 cm^{-1} . However, the fingerprint region below, which comprises many relevant vanadium–oxygen vibrations^[22] and the higher wavenumber region that contains the important carbon-related modes,^[23] was not resolved.

This article reveals the oxidation kinetics of dissolved vanadium ions on graphite electrodes. Using the widely studied model materials graphene and highly ordered pyrolytic graphite (HOPG), the differences of reaction kinetics were explicitly investigated based on the structural and electrocatalytic properties of the electrode. Variation of laser excitation energy showed that adsorbents and reaction intermediates are sensitive to the wavelength used and can only be detected under optimized analytical conditions. The specific use of modified electrodes allowed the detection of the buildup of vanadium complexes directly at the interface between electrolyte and edge-exposed graphite, including electrolyte products and reaction intermediates.

[a] Dr. H. Radinger, F. Bauer, Dr. F. Scheiba
Institute for Applied Materials
Karlsruhe Institute of Technology
Hermann-von-Helmholtz-Platz 1,
76344 Eggenstein-Leopoldshafen (Germany)

[b] Dr. H. Radinger
Department of Chemical and Process Engineering
University of Canterbury
8140 Christchurch (New Zealand)
E-mail: hannes.radinger@canterbury.ac.nz

 Supporting information for this article is available on the WWW under
<https://doi.org/10.1002/batt.202200440>

 © 2022 The Authors. *Batteries & Supercaps* published by Wiley-VCH GmbH.
This is an open access article under the terms of the Creative Commons Attribution Non-Commercial License, which permits use, distribution and reproduction in any medium, provided the original work is properly cited and is not used for commercial purposes.

Results and Discussion

Raman spectra of electrolyte and electrodes

Prior to a meaningful analysis of the spectra recorded under *operando* conditions, we studied the dissolved vanadium oxide species separately in sulfuric acid. A systematic analysis of the characteristic scattering pattern of each component allows the assignment of new signals for the identification of reaction intermediates and products. Figure 1(a and b) shows the electrolyte used on the positive side of a vanadium flow battery in the uncharged and charged/oxidized states compared to the salt and sulfuric acid used to prepare the solutions; Table 1 lists the observed modes and their assignment. Strong signals correspond to the symmetric stretching of HSO_4^- (590 cm^{-1} and 1050 cm^{-1}), and the total symmetric stretching of SO_4^{2-} (985 cm^{-1}). The weak asymmetric stretching of HSO_4^- and its overtone are located at 895 and 1085 cm^{-1} , respectively.^[24–26]

Solid vanadyl sulfate shows three intense signals related to symmetric stretching of V=O (1000 cm^{-1}), and the symmetric and asymmetric S–O stretching of SO_4^{2-} tetrahedra at 1025 and 1115 cm^{-1} , respectively (Figure 1a). The region from 610 to 680 cm^{-1} has weakly observable peaks associated with hydrated vanadium sulfate ions; features at

475 and 270 cm^{-1} belong to the bending vibrations of O–S–O and O–V–O bonds.^[27] In its dissolved state, a merged signal of at least two peaks just below 1000 cm^{-1} is visible. The broadening of the signals and the shift in their position can be attributed to the solvation of the ions, *i.e.*, their new coordination environment of water and sulfate species.^[28] The band at 990 cm^{-1} arises from a stretching vibration of the V=O bond in the vanadyl-aqua complex,^[29,30] whereas the sharper signal at 980 cm^{-1} results from the symmetric stretching of a sulfate ion in the second coordination sphere of the hydrated complex.

V_2O_5 powder was used to resolve the structure of undissociated pentavalent vanadium (Figure 1b). The strongest signal at 995 cm^{-1} corresponds to the symmetric stretching of V=O bonds. A symmetric and asymmetric part of a V–O–V vibration at 525 and 700 cm^{-1} defines the dimeric structure of V_2O_5 .^[31] At 955 cm^{-1} a second bridging vibration, formed through another oxygen atom, is recognized, which is weak due to its low polarizability. Stretching and bending vibrations of V–O–V structures are noted at 480 and 400 cm^{-1} .^[32] At 280 and 300 cm^{-1} common modes of parallel vanadium oxide chains are responsible for the distortion and puckering of the so-called ladder.^[22] The interactions of ions with the aqueous solvation shell again

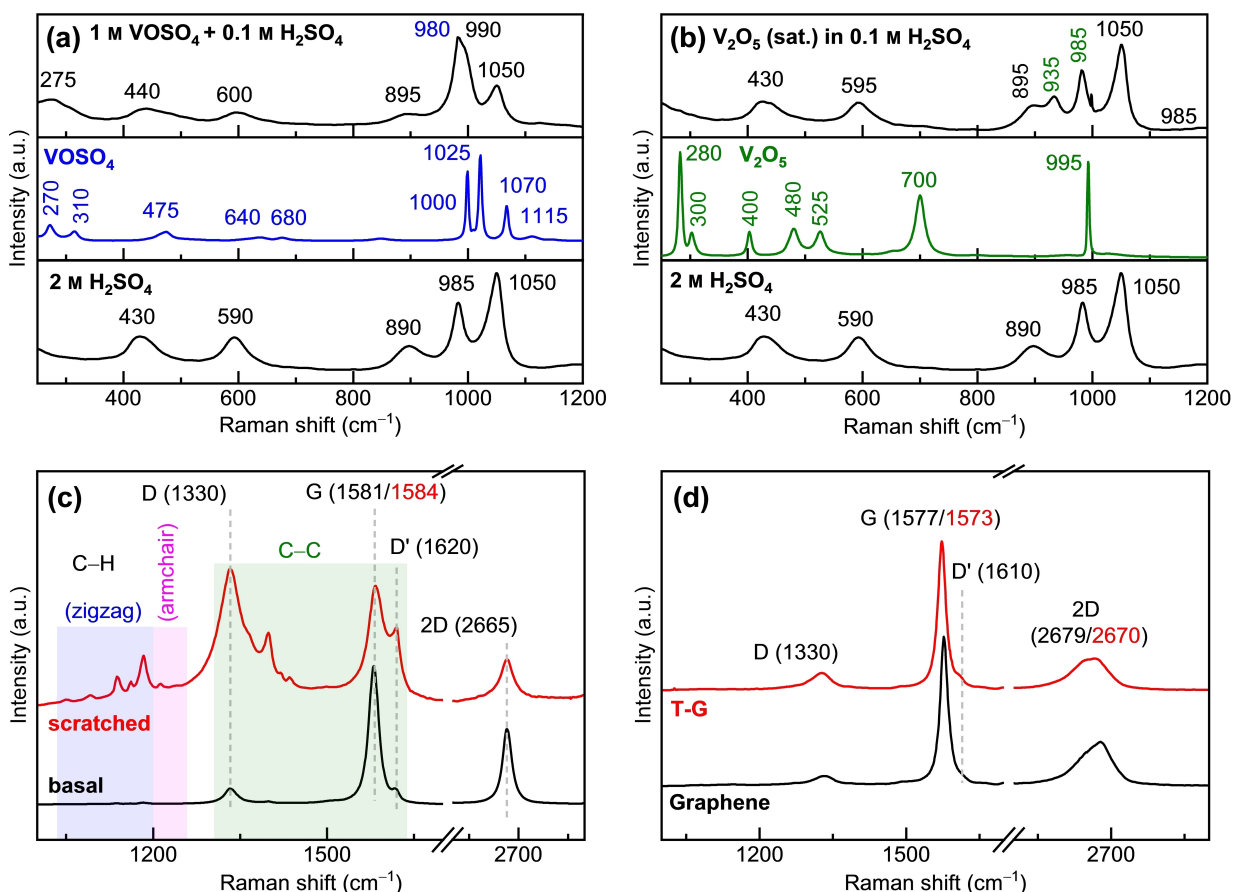


Figure 1. Raman spectra of solid and dissolved vanadium oxides and the carbon-based substrates used. a) Uncharged and b) charged positive electrolytes compared to their corresponding salts and sulfuric acid. c) HOPG exposing the basal plane and after being scratched; d) pristine and tetracene modified graphene (T–G).

Table 1. Position and assignment of the peak in the Raman spectra in Figure 1 of sulfuric acid and vanadium sulfate and vanadium oxide, respectively, as solid powder and dissolved in sulfuric acid. Peak values of solid samples are given in brackets.

H ₂ SO ₄ Peak [cm ⁻¹]	Assignment	VOSO ₄ in H ₂ SO ₄ (solid) Peak [cm ⁻¹]	Assignment	V ₂ O ₅ in H ₂ SO ₄ (solid) Peak [cm ⁻¹]	Assignment
430	$\delta_{as}(SO_3)$	(270)/275	$\delta(O-S-O)/\text{hydrated}$	(280)	$\delta(O-V-O)$
		(310)	n/a	(300)	$\nu_s(V=O)$
590	$\nu_s(HSO_4^-)$	440	$\delta_{as}(SO_3)$	(400)	$\delta(V-O-V)$
		(475)	$\delta(O-S-O)/ \delta(O-V-O)$	(430)	$\delta_{as}(SO_3)$
890	$\nu_{as}(HSO_4^-)$	600	$\nu_s(HSO_4^-)$ near V ^{IV} O ²⁺	(480)	$\nu_s(V=O-V)$
		(610-680)	VOSO ₄ +H ₂ O	(525)	$\nu_s(V=O)$
985	$\nu_s(SO_4^{2-})$	900	$\nu_{as}(HSO_4^-)$	(595)	$\nu_s(HSO_4^-)$ near V ^{IV} O ₂ ⁺
		935	$\nu_s(V=O)$ in V ^{IV} O ₂ ⁺	(700)	$\nu_{as}(V-O-V)$
1050	$\nu_s(HSO_4^-)$	980	$\nu_s(SO_4^{2-})$ near V ^{IV} O ²⁺	895	$\nu_{as}(HSO_4^-)/\nu_{as}(V=O)$
		990	$\nu_s(V=O)$	935	$\nu_s(V=O)$
1085	$\nu_{as}(HSO_4^-)$	(1000)	$\nu_s(V=O)$	(955)	$\nu_s(V-O-V)$
		(1025)	$\nu_s(SO_4^{2-})$	985	$\nu_s(SO_4^{2-})$
		(1070)	$\nu_{as}(SO_4^{2-})$	(995)	$\nu_s(V=O)$
		(1115)	$\nu_{as}(SO_4^{2-})$	1020	$\nu_s(HSO_4^-)$ near V ^{IV} O ₂ ⁺

results in a broadening and shifting of spectral features for the dissolved salt. Several intense features at 595, 900, 1050, and 1090 cm⁻¹ can be associated with H₂SO₄, since a higher concentration had to account for the low solubility of V₂O₅. A strong peak at 935 cm⁻¹ corresponds to a symmetric V=O vibration and at 1020 cm⁻¹, the vibration of V^{IV}O₂⁺ against SO₄²⁻ anions in its second coordination sphere is observed.^[33] Due to the complexity of the different signals, it is not always easy to separate salt and solvent. At 895 cm⁻¹, e.g., an HSO₄⁻ stretching overlaps with the asymmetric stretching of the V^{IV}O₂⁺ ion.^[34]

To draw reliable conclusions about the processes that occur at the solid–liquid interface, not only must the dissolved electrolyte species but also the signals from the carbonaceous electrode be known. We selected HOPG as a model system to directly compare basal and edge planes of graphite, and, according to our previous study, zigzag edge modified graphene to specifically address the effect of highly active edge sites.^[35] The basal plane of HOPG reveals an intense G and 2D band at 1581 and 2665 cm⁻¹, along with weaker defect-related features at 1330 and 1620 cm⁻¹ for the D and D' bands (Figure 1c). In contrast, for edge-plane exposed HOPG, the signals originating from the latter are very strong. In addition, it is possible to distinguish between zigzag and armchair geometries for edge regions, as shown theoretically and experimentally.^[36] While up to 1200 cm⁻¹ signals from zigzag edges are predominant, above that the orientation of the armchair becomes apparent; both are present on the scratched HOPG to a not quantifiable extent. The modification of graphene by a monolayer of zigzag nanoribbons (T-G) is not sufficient to make these features visible in the spectra (Figure 1d). Instead, the higher number of edges shows only a slight increase in the relative intensity of the D compared to that of the G band. The disruption of the graphene layer stacking by the nanoribbon shifts the G band to lower and the 2D band, which shows peak splitting due to the additional layer, to higher wavenumbers.

Electrocatalytic activity of the substrates

Cyclic voltammetry (CV) curves were recorded to investigate the possible potential range in which different spectral changes will be suspected in the *operando* measurements. An active electrocatalyst reduces the overpotential required for V^{IV}O₂⁺/V^{IV}O²⁺ oxidation as close to the thermodynamic minimum as possible. This can be demonstrated by comparing HOPG exposed to the electrolyte before and after carving of the basal plane. Only for the latter sample does the CV show a clear oxidation wave before a steep current rise resulting from carbon corrosion, while for the inactive basal plane, these two signals blend into each other (Figure 2a). The edge-rich HOPG also shows the dependence of the electrocatalytic activity for vanadium oxidation on graphitic defects.

Both the pristine and modified graphene possess a characteristic double-peak structure, resulting from variations in the activity of the basal plane and edge regions (Figure 2b). It is found that the synthetic edges outperform not only the natural activity of graphene by shifting both oxidation waves to lower potentials, but also the HOPG exposed at the edges. A detailed study of the surface chemistry and electronic structure of graphene modified by polycyclic aromatic hydrocarbons as well as pristine and damaged HOPG can be found elsewhere.^[35] Briefly explained, increased activity was not related to a change in surface oxygen content, but additional edge sites reduce the work function of the electrode, which is beneficial for vanadyl oxidation. The electrochemical measurements identified two sample types diverging in electrocatalytic activity for each material class, which thus allows meaningful comparison of spectral differences under working conditions. The optical characteristics in the following can finally be associated with potential-dependent conversion products of electrolyte species according to Figure 1a,b, intrinsic variances in the electrode structure as shown in Figure 1(c and d), or unknown surface reaction intermediates as a result of electrocatalytic activity (Figure 2).

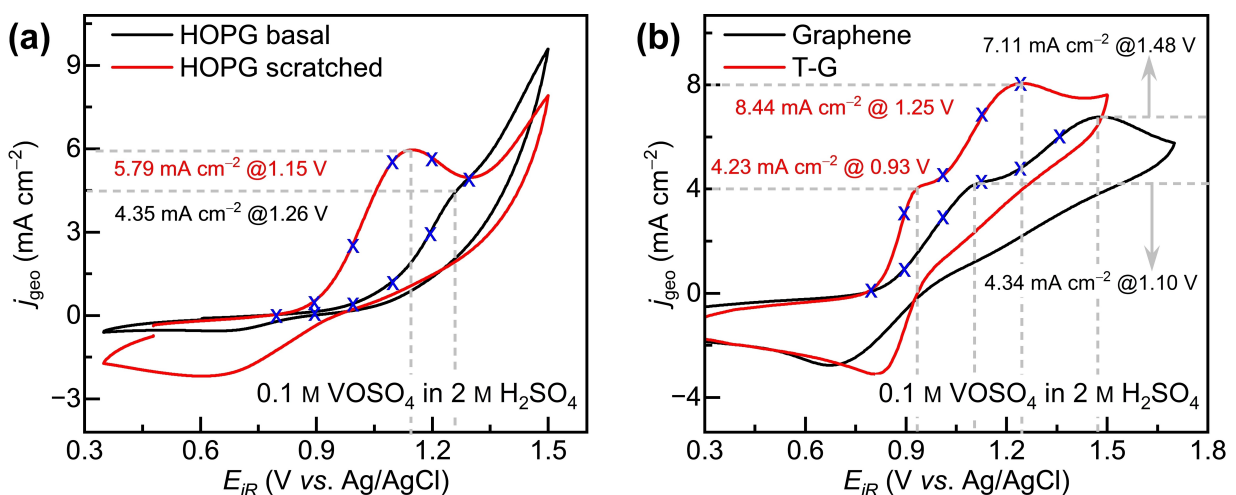


Figure 2. Electrocatalytic activity of the graphite-based substrates used. a) Basal plane exposed and scratched HOPG. b) Pristine and tetracene modified graphene.

Operando Raman spectra

Two different laser wavelengths were used to find a compromise between signal intensity and spectral resolution of the Raman features. Although the lower wavelength of green light (532 nm) usually provides higher intensity for low cross-sectional area modes, the red laser (633 nm) is often preferred for carbon-based materials as it offers higher resolution of overlapping, especially defect-related peaks.^[37] The concentration of H_2SO_4 in our experiments was reduced from 2 mol L^{-1} , which is usually used in catalytic measurements and real cells, to 0.1. In Figure 1, it was observed that the signals of sulfuric acid are strong even at low concentrations, masking bands from dissolved species. Because of the lowered concentration, the pH of the electrolyte increases from 0 to 1. While this still has a relatively low effect on the coordination of the vanadium ions in solution, a further decrease to, e.g., 1 mM would shift the pH to about 3, which dramatically influences the concentration of H^+ , HSO_4^- , and SO_4^{2-} complexes in the electrolyte and thus would not allow reliable extrapolation of our results towards the processes in a battery cell.^[38]

To investigate the kinetics at graphitic defects, we studied freshly cleaved and scratched HOPG. Figure 3(a) presents the Raman spectra for HOPG exposed in the basal plane, showing the transition from symmetric stretching of the $\text{V}=\text{O}$ bond in $\text{V}^{\text{IV}}\text{O}^{2+}$ (981 cm^{-1}) to the double-peak structure formed by symmetric and asymmetric stretching of the $\text{V}^{\text{V}}\text{O}_2^+$ ion (933 and 895 cm^{-1}) at a high potential of 1.3 V vs. Ag/AgCl. Spectra below 500 cm^{-1} cannot be evaluated due to high fluorescence, overshadowing possible signals in that range (Figure S1). A weak signal from the interaction of the pentavalent vanadium ion with H_2SO_4 occurs at $\sim 860 \text{ cm}^{-1}$. Residual characteristics, if present, are of such low intensity that further interpretation is not reliable, as it is shown in Figure S2. The new features that appeared after prolonged amperometry at 1.3 V could be attributed to the onset of substrate oxidation, which occurred at lower potentials for basal plane exposed HOPG during CV

(compare Figure 2a). Small defects created by the oxidation serve as active site for the vanadyl oxidation. Direct comparison with the spectra of scratched HOPG in Figure 3(b) reveals two increasing signals at 935 and 895 cm^{-1} at only 1.0 V vs. Ag/AgCl, consistent with the higher electrocatalytic activity (Figure 2a). The peak transition in this wavenumber range can therefore be considered as an activity indicator that sets in at the edges at earlier potentials than in the basal plane.

Due to fluorescence occurring below 500 cm^{-1} and the static carbon signals, the spectra of scratched HOPG were again measured with a lower laser excitation energy (Figure 3c). From 0.9 V vs. Ag/AgCl, the symmetric (930 cm^{-1}), followed by the asymmetric stretching of $\text{V}^{\text{V}}\text{O}_2^+$ (900 cm^{-1}) occurs at slightly higher potentials. As a new weak feature between the stretching of $\text{V}=\text{O}$ in $\text{V}^{\text{IV}}\text{O}^{2+}$ (980 cm^{-1}) and HSO_4^- , a newly discovered band at 1020 cm^{-1} is associated with the interaction between $\text{V}^{\text{V}}\text{O}_2^+$ and SO_4^{2-} anions.^[34] Complementing the known pentavalent vibrational modes, there is a feature at 707 cm^{-1} that originates from the asymmetric stretching of the $\text{V}-\text{O}-\text{V}$ bonds. It is accompanied by a weak shoulder at $\sim 670 \text{ cm}^{-1}$ and its symmetric part at $\sim 510 \text{ cm}^{-1}$, which cannot be related to the V_2O_5 powder (Figure 1b).

The possibility that the energy input from the laser exposure led to the precipitation of oxidized vanadium compounds could be ruled out for three reasons: the observed pattern could be (i) reliably reproduced at other locations on the electrode that had not been previously illuminated, and (ii) successfully reversed by lowering the potential at the same location (Figure S3). At a reversal potential of 0.8 V , features of both $\text{V}^{\text{IV}}\text{O}^{2+}$ and $\text{V}^{\text{V}}\text{O}_2^+$ were visible, but at 0.6 V vs. Ag/AgCl, the modes originating from the uncharged electrolyte were observed. (iii) In previous experiments, a green laser with higher energy was used. Nevertheless, no signals indicative of solid V_2O_5 were detected in these cases.

The observed low wavenumber pattern that develops at potentials above 1.0 V vs. Ag/AgCl is best described by the vibrational bands of $\beta\text{-V}_2\text{O}_5$ that can be generated by applying

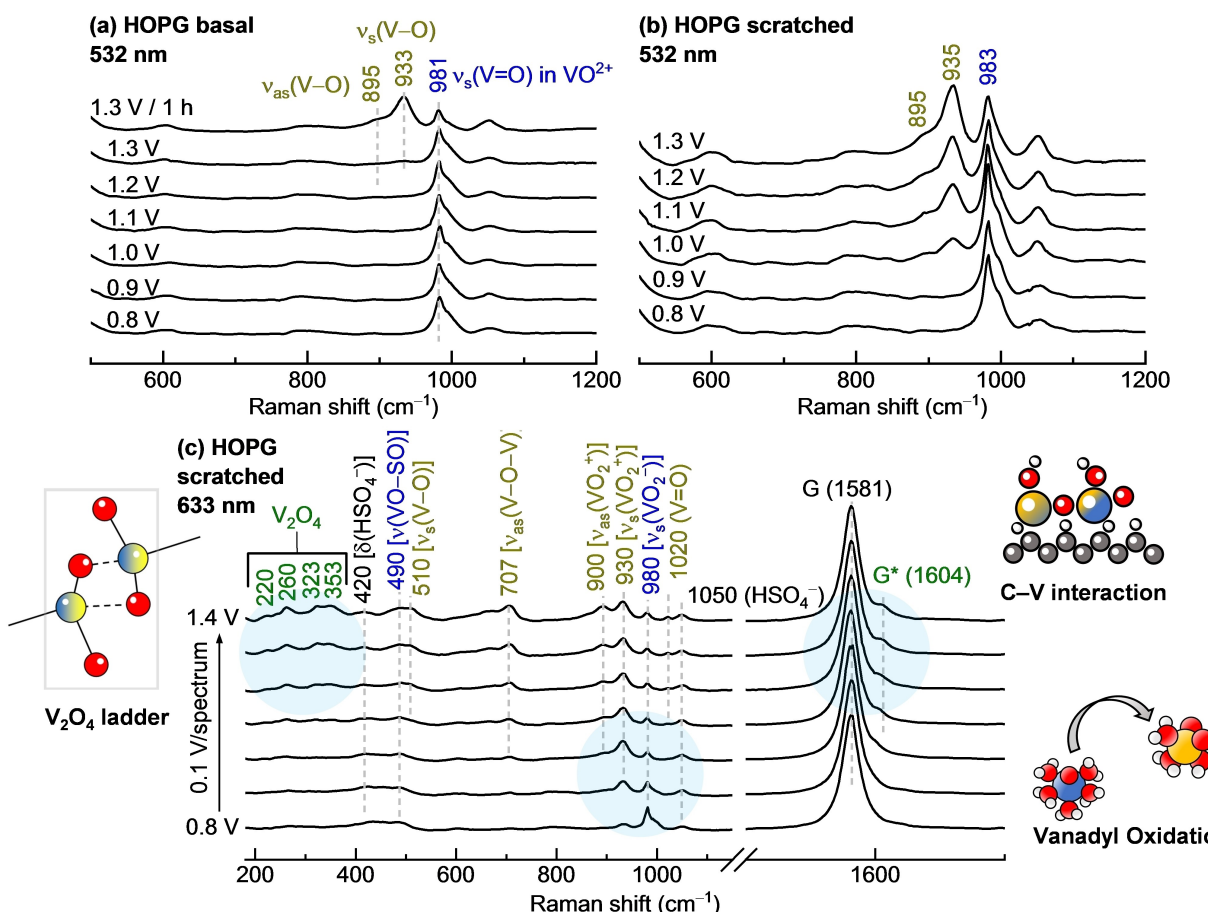


Figure 3. Stacked operando Raman spectra of HOPG. a) Basal plane exposed and b) scratched HOPG recorded with a laser wavelength of 532 nm; c) scratched HOPG recorded with a wavelength of 633 nm. All potential values are given vs. Ag/AgCl.

temperatures above 200 °C and high pressures up to 8 GPa to α -V₂O₅.^[22,39] All V₂O₅ polymorphs can be considered as an assembly of VO_x polyhedral, but while the alpha phase consists of VO₅ structures, vanadium is coordinated 6-fold in the beta phase. Crystallographic and theoretical data defined the latter as parallel chains of V₂O₄, held together by weak interactions, justifying its designation as V₂O₅.^[39] All features observed below 400 cm⁻¹ can be associated with the distortion of these V₂O₄ ladders.^[22]

The double peak structure at 323 and 353 cm⁻¹ corresponds to an in-plane stretching of a V=O bond (323 cm⁻¹) and two oxygen atoms in the coordination sphere of a vanadium center (353 cm⁻¹) as ladder breathing (Figure 3c).^[39,40] The vibration at 260 cm⁻¹ originates from an in-plane vibration of an edge-shared oxygen (lit.: 243 to 253 cm⁻¹) or from an out-of-plane motion of the V–O–V bond (lit.: 271 to 272 cm⁻¹).^[39,40] With similar uncertainty, the 220 cm⁻¹ mode can be associated with in-plane stretching of V=O (lit.: 220 to 222 cm⁻¹) or displacement of adjacent layers (lit.: 228 cm⁻¹).^[39,40] Assignment of such low-wavenumber modes is generally difficult, especially since the instability of numerous V₂O₅ polymorphs under ambient conditions complicates experimental characterization. Intense ladder modes of atmospherically stable α -V₂O₅ are found at lower wavenumbers of 285 and 305 cm⁻¹, which

excludes its presence and thus precipitation.^[39] Additionally, distinct features at 406, 483, and 528 cm⁻¹, which are characteristic for α -V₂O₅, are absent.

The modes could also be described by γ' -V₂O₅, whose structure is very similar to β -V₂O₅, but without the translational equivalence of adjacent layers.^[41] Its ladder modes lie at 350 and 333 cm⁻¹, originating from the in-plane vibration of vanadium atoms, the distortion of vanadium along the chain at ~260 cm⁻¹, and the out-of-plane motion of oxygen in the V–O–V bond at ~220 cm⁻¹.^[41] Regardless of the final classification, vanadium species are considered to be dimeric, *i.e.*, they consist of two VO₂ ions connected by an oxygen bridge. From the Pourbaix diagram of vanadium, it is clear that no covalently bonded V₂O₄ species can exist at the applied potential within a pH of < 1. It is only because of their proximity at the electrode that they appear as a ladder species, which is otherwise found in crystalline V₂O₅.

Reaction intermediates of dimeric origin were previously postulated, assuming that they occur at oxygen groups on the electrode.^[13] However, in our case, there were none of these potential-dependent changes between 740 and 820 cm⁻¹ associated with the interaction of vanadium and surface oxygen. In fact, at the start of the experiment several overlapping features at approximately 800 cm⁻¹ are visible, which

are not present for H_2SO_4 or vanadium oxide/vanadyl sulfate (see Figure S4 and compare with Figure 1a and b). It can thus be assumed that these features arise due to the interaction of dissolved species with the graphite surface. However, as the potential increases and the intermediates appear, the bands vanish, revealing no pattern distinguishable from the background signal. Finally, only experiments that detect the changing surface chemistry under an applied potential could reveal the presence or absence of oxygen groups during the electron transfer reaction. Our previous studies, which e.g., revealed indistinguishable oxygen content on differentially active graphite electrodes after polarization in the positive half-cell,^[20] in conjunction with the Raman data proposed here, suggest that charge transfer is more likely to occur at unoxidized defect sites.

Instead, carbon-related vibrations reveal an altered shape at oxidative potentials (Figure 3c): a shoulder above the G mode at 1604 cm^{-1} , referred to as G^* , occurs simultaneously with electrolyte conversion. Its origin could theoretically have two reasons: i) changes in the local electronic structure resulting from the presence of charged species such as vanadium ions lead to a shift in the G band, as it can also be observed in the doping of graphene.^[42–44] ii) Intercalation of ions, such as H_2SO_4 , between graphite layers, causing a splitting of the G band because of an increased force constant of the graphite lattice.^[45–47] To clarify this conflict, graphene was employed as an electrode since it provides multiple intercalation sites. For the green laser, the transition of the electrolyte species above 1.2 V vs. Ag/AgCl is observed without additional changes in the carbon components (Figure S5). The spectral change, however, is accompanied by a growing G^* band at $\sim 1600 \text{ cm}^{-1}$ when the sample is illuminated with red light (Figure S6). The wavelength sensitivity of the feature can already be associated with a surface process and not with intercalation, as the latter effect does not depend on the excitation energy.^[48] Further measurements in H_2SO_4 only definitely exclude intercalation, since no

spectral changes were observed over the entire potential range with the red laser (Figure S7). The growth of the G^* band is therefore interpreted as an electronic interaction between the carbon atoms in the graphite structure and the vanadium ions from the electrolyte.

Finally, to distinguish between oxidized electrolyte species and reaction intermediates, the measurement in Figure 3(c) was repeated at an edge-free location directly adjacent to the previously characterized scratched sites. A transformation of electrolyte species at 937 cm^{-1} already occurs at about 1.0 V vs. Ag/AgCl, as was the case for the edge-related spectra, but not for the previously characterized basal plane (Figures 3a and S8). Oxidized $\text{V}^{\text{IV}}\text{O}_2^+$ ions thus diffuse from the active site at the edge to the spot illuminated by the laser. No other vibrational characteristics were detected and no potential-dependent structural changes associated with carbon were visible, which allowed two conclusions: (i) the ladder vibrations and possibly the V–O–V mode at 707 cm^{-1} belong to a reaction intermediate formed during the oxidation of $\text{V}^{\text{IV}}\text{O}_2^+$, and (ii) the growing G^* band demonstrates the interaction of vanadium ions with graphite at graphitic edge sites only, which is crucial for charge transfer.

Additional *operando* Raman spectra were recorded for zigzag edge-modified graphene (T–G) to verify the conclusions about edge-related reaction intermediates. In order to decrease electrolyte-induced signals while improving the resolution of intermediates, the concentration of dissolved species was reduced from 1 to 0.1 M VOSO_4 in 0.1 M H_2SO_4 . Consequently, the overall spectrum at low potentials is dominated by H_2SO_4 features (Figure 4a). At 1.1 V vs. Ag/AgCl, the stretching of HSO_4^- at 890 cm^{-1} is accompanied by two asymmetric stretching vibrations associated with $\text{V}^{\text{IV}}\text{O}_2^+$ ions at 867 and 895 cm^{-1} , indicating electrolytic transformation by the oxidation of $\text{V}^{\text{IV}}\text{O}_2^+$. In comparison to scratched HOPG the signals of pentavalent vanadium arise at higher potentials. Considering the current onset at about 0.9 V vs. Ag/AgCl during CV

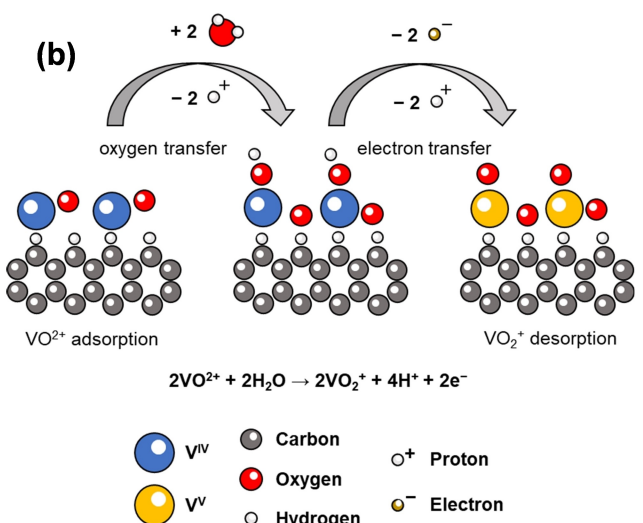
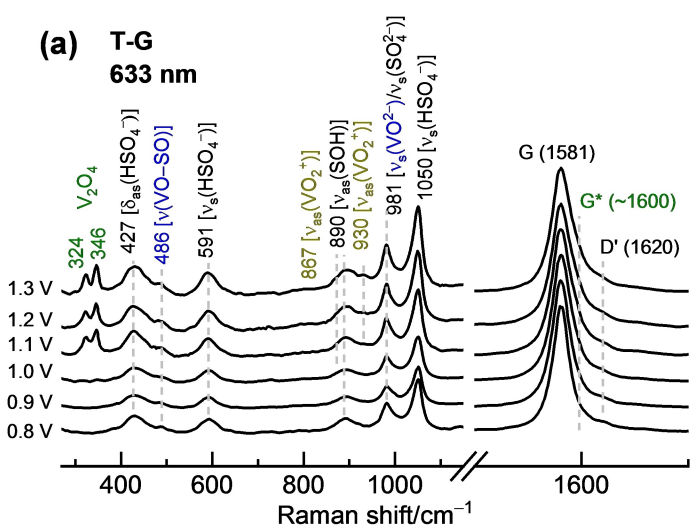


Figure 4. Vanadyl oxidation at graphitic zigzag edge sites. a) Stacked *operando* Raman spectra of T–G recorded with a laser wavelength of 633 nm; b) reaction mechanism of dimeric vanadyl species for the formation of pentavalent vanadium oxide.

(Figure 3b), this can be related to the lower concentration of vanadium species, whose signal is buried beneath the H_2SO_4 pattern. Furthermore, the V–O–V and V–O vibrations at about 500 cm^{-1} cannot be observed due to their overlap with the VO–SO stretching of the educt. The asymmetric V–O–V bridge stretching and its shoulder at about 700 cm^{-1} cannot be addressed with certainty as well. Apart from that, a pronounced double-peak structure associated with the V_2O_4 ladder modes at 324 and 346 cm^{-1} is a strong indicator for the presence of adsorbed dimeric species at edge sites during the reaction. Again, no additional spectral features associated with the interaction of vanadium ions with surface oxygen were observed. Instead, a growing G^* band at $\sim 1600 \text{ cm}^{-1}$ at higher potentials proves the direct interaction of vanadium with the edges of the electrode. It can further be seen that the G^* band exists independent of the defect-related D' band, which can be found at about 1620 cm^{-1} .

Based on our results for HOPG and zigzag edge modified graphene, we propose a kinetic mechanism for vanadyl oxidation in sulfuric acid (Figure 4b). We previously found that a larger π -conjugated system improves the edge site related oxidation kinetics of the reaction. The *operando* Raman data suggest that this corresponds to the presence of vanadium dimers, which need sufficient space to adsorb and react at graphite. After the adsorption of two neighboring VO_2^+ complexes, two OH groups covalently bond to the adsorbed vanadium ions under the release of two protons from surrounding H_2O molecules in the coordination sphere. Due to electron transfer towards the substrate, two outstanding H^+ desorb, forming two close VO_2^+ species, which then desorb to free the reaction site. We acknowledge that our scheme represents a simplified version of the actual occurrences at the electrode. It is clear that the proposed transfer of two OH groups, the release of two protons, the transfer of two electrons, and the desorption of two more protons do not occur in just two steps. However, to avoid a complex eight-step reaction scheme, we have grouped these processes.

Conclusion

In this work, *operando* Raman spectroscopy was used to follow the electrocatalytic oxidation from $\text{V}^{\text{IV}}\text{O}^{2+}$ to $\text{V}^{\text{V}}\text{O}_2^+$, which is considered one of the kinetic bottlenecks in vanadium flow batteries. By a systematic analysis of all solid and dissolved compounds involved, the resulting signals and potential-dependent structural changes were successfully separated and related to the oxidation of the electrolyte, the reaction intermediates, and the interactions of vanadium ions and carbon atoms. The oxidation of dissolved vanadium species can be followed by a transition of vibrational bands associated with $\text{V}^{\text{V}}\text{O}_2^+$ instead of $\text{V}^{\text{IV}}\text{O}^{2+}$ complexes just below 1000 cm^{-1} , whose starting potential corresponds to the electrocatalytic activity of the electrode. Furthermore, several vibrations were observed in the active edge regions below 500 cm^{-1} , related to the ladder modes of the V_2O_4 structures, suggesting reaction intermediates of dimeric origin. No previously ascribed inter-

action with surface oxygen was observed for active electrodes. Instead, an additional signal was visible above the graphite-related G band at $\sim 1600 \text{ cm}^{-1}$, corresponding to the direct electronic interaction of carbon atoms from the substrate and vanadium ions in the electrolyte. In summary, vanadium ions primarily react directly at nonfunctionalized zigzag carbon edge sites of sufficient size as dimeric species.

Experimental Section

Sample preparation

The basal plane of HOPG was prepared by cleaving the topmost layer using a conventional tape. Edge planes were introduced by carefully scratching the surface of freshly cleaved HOPG with few parallel lines using a scalpel (Figure S9). Defect-free graphene (Dasheng graphene Co. Ltd., China) was used as a substrate to produce a model catalyst with zigzag edge sites using tetracene (Sigma Aldrich, $\geq 99\%$ purity) according to the literature.^[49] Tetracene and graphene were dispersed in dimethyl sulfoxide under ultrasound and stirred overnight. The product was filtered, washed with Milli-Q several times to remove excess hydrocarbons and solvent, and dried at 80°C . To prepare a dispersion for electrochemical measurements, 4 mg of the product were ultrasonicated in a mixture of 390 μL IPA and 10 μL Nafion (5 wt%, Sigma-Aldrich).

Electrochemical measurements

As an electrolyte to collect electrocatalytic data via cyclic voltammetry ($v = 20 \text{ mVs}^{-1}$), 0.1 M $\text{V}^{\text{IV}}\text{O}^{2+}$ was prepared by dissolving VOSO_4 powder (Alfa Aesar) in 2 M H_2SO_4 (Emsure). Graphite felt was used as counter, and Ag/AgCl stored in 3 M KCl ($E_{\text{Ag}/\text{AgCl}} = 0.210 \text{ V}$ vs. RHE) as reference electrode. A custom-built sample holder was used to acquire the electrochemical data of thin HOPG plates, exposing either the freshly cleaved basal or the scratched edge plane to the electrolyte with a PTFE mask. 10 μL of the model catalyst was drop coated on PEEK-encased glassy carbon (ALS) and measured in a glass vessel, using the same reference specified above and a graphite rod (redox.me) as counter electrode. Before coating, the glassy carbon was polished on a cloth using aluminum suspension (Buehler, 0.5 μm), before being ultrasonically cleaned in IPA and Milli-Q. An iR drop of 3 to 4 Ω was assessed by impedance spectroscopy at the open circuit potential and used to correct electrochemical measurements.

Raman spectroscopy

The degree of disorder was investigated by Raman spectroscopy, using a LabRAM HR Evolution spectrometer (HORIBA scientific), equipped with a HeNe laser ($\lambda = 632.8 \text{ nm}$, $E = 1.9876 \text{ eV}$) and a 532 nm Nd:YAG laser ($E_{\text{laser}} = 2.33 \text{ eV}$). A 600 grooves mm^{-1} grating along with a 50 \times magnification (NA = 0.5) objective was employed, resulting in a spot size of about 2 μm . The Raman spectra of the electrolytes were measured by placing a drop of the solution (background: 2 M H_2SO_4 , electrolyte: 1 M VO^{2+} in 0.1 M H_2SO_4 , oxidized electrolyte: sat. VO_2^+ in 0.1 M H_2SO_4) on a microscope slide. The samples were irradiated for acquisition times of 20 to 60 s, accumulating 3 spectra. All spectra were background corrected with a spline baseline using the software CasaXPS. However, no deconvolution or line smoothing was undertaken to omit falsification of the results. Therefore, we consciously neglected

the peak pitting of our data to not over-eagerly analyze features below the clear visibility of the naked eye.

Operando spectra were monitored using a commercial Raman cell (TSC Raman, rhd instruments, scheme in Figure S10). A gold-coated copper ring is used as counter, Ag/AgCl (3 M KCl) as reference electrode. As electrolyte, 1 M VO_2^{+} in 0.1 M H_2SO_4 was used if not mentioned otherwise. The design of the cell theoretically allows a monolayer of electrolyte to form between the electrode and the glass slide due to capillary forces. At the beginning of a measurement, several points on the sample were tested with respect to the signal intensity ratio between carbon (D, G) and electrolyte-related signals to find the optimum height and focus on the electrode-electrolyte interface. Subsequently, a potential of 0.6 V vs. Ag/AgCl was applied for about 10 min. Afterwards, the potential was increased from 0.8 to 1.4 V vs. Ag/AgCl in steps of 0.1 V. Chronoamperometry curves were recorded to trace the stabilization of the current response (Figure S11). After about 60 s, a Raman spectrum was acquired, accumulating three measurements of about 20 to 30 s. In this manner, it can be assured that a stable system is investigated and no or only minor changes of the material occur. Furthermore, the diffusion of ionic species towards/away from the surface are constant, thus not altering Raman signals due to a changing concentration of vanadium species. At a stabilized current, a reproducible Raman pattern can be recorded multiple times.

A gold coin (Schiefer Co., 99.9% purity) was used as a substrate and current collector during the measurements. Cleaved and scratched HOPG (5×5 mm) was placed on top of the gold coin. To guarantee wetting of these defects, electrolyte was dropped onto HOPG and pressed into the channels with a glass plate before the sample was assembled. Carbon dispersions were evaluated by dropping them onto gold coins using a spin coater (Raman baseline of gold in Figure S12). 10 μL of the dispersion was added onto the rotating gold disk before it was dried for several hours at room temperature. Only tiny particles invisible to the human eye remained on the substrate. Therefore, changes in electrolyte concentration are not expected to dramatically affect the spectra.

Acknowledgements

The financial support by the German Federal Ministry of Education and Research within the project Flow3DKat (03EK3053 C) is gratefully acknowledged. This work contributes to the research performed at CELEST (Center for Electrochemical Energy Storage Ulm-Karlsruhe). Open Access funding enabled and organized by Projekt DEAL.

Conflict of Interest

The authors declare no conflict of interest.

Data Availability Statement

The data that support the findings of this study are available from the corresponding author upon reasonable request.

Keywords: electrocatalysis · graphite electrodes · operando Raman spectroscopy · reaction mechanism · vanadium flow batteries

- [1] B. M. Weckhuysen, *Chem. Commun.* **2002**, 2, 97.
- [2] M. A. Bañares, M. O. Guerrero-Pérez, J. L. G. Fierro, G. G. Cortez, *J. Mater. Chem.* **2002**, 12, 3337.
- [3] V. Calvino-Casilda, M. A. Bañares, in *Catalysis*, Vol. 24 (Eds.: J. J. Spivey, M. Gupta), Royal Society of Chemistry, Cambridge 2012, p. 1.
- [4] S. Damyanova, L. M. Gomez, M. A. Bañares, J. L. G. Fierro, *Chem. Mater.* **2000**, 12, 501.
- [5] M. O. Guerrero-Pérez, M. A. Bañares, *Catal. Today* **2006**, 113, 48.
- [6] I. E. Wachs, C. A. Roberts, *Chem. Soc. Rev.* **2010**, 39, 5002.
- [7] H. Radinger, P. Connor, R. Stark, W. Jaegermann, B. Kaiser, *ChemCatChem* **2021**, 13, 1175.
- [8] H. Radinger, P. Connor, S. Tengeler, R. W. Stark, W. Jaegermann, B. Kaiser, *Chem. Mater.* **2021**, 33, 8259.
- [9] M. Inaba, H. Yoshida, Z. Ogumi, *J. Electrochem. Soc.* **1996**, 143, 2572.
- [10] M. Anji Reddy, M. Helen, A. Groß, M. Fichtner, H. Euchner, *ACS Energy Lett.* **2018**, 3, 2851.
- [11] I. Oda, H. Ogasawara, M. Ito, *Langmuir* **1996**, 12, 1094.
- [12] B. D. Smith, D. E. Irish, P. Kedzierszawski, J. Augustynski, *J. Electrochem. Soc.* **1997**, 144, 4288.
- [13] N. A. Gvozdik, K. J. Stevenson, *Electrochim. Acta* **2021**, 383, 138300.
- [14] I. Kroner, M. Becker, T. Turek, *ChemElectroChem* **2020**, 7, 4314.
- [15] B. Sun, M. Skyllas-Kazacos, *Electrochim. Acta* **1992**, 37, 2459.
- [16] L. Yue, W. Li, F. Sun, L. Zhao, L. Xing, *Carbon* **2010**, 48, 3079.
- [17] W. Zhang, J. Xi, Z. Li, H. Zhou, Le Liu, Z. Wu, X. Qiu, *Electrochim. Acta* **2013**, 89, 429.
- [18] X. W. Wu, T. Yamamura, S. Ohta, Q. X. Zhang, F. C. Lv, C. M. Liu, K. Shirasaki, I. Satoh, T. Shikama, D. Lu, S. Q. Liu, *J. Appl. Electrochem.* **2011**, 41, 1183.
- [19] M. Park, I.-Y. Jeon, J. Ryu, J.-B. Baek, J. Cho, *Adv. Energy Mater.* **2015**, 5, 1401550.
- [20] H. Radinger, A. Ghamlouche, H. Ehrenberg, F. Scheiba, *J. Mater. Chem. A* **2021**, 9, 18280.
- [21] H. Radinger, J. Pfisterer, F. Scheiba, H. Ehrenberg, *ChemElectroChem* **2020**, 7, 4745.
- [22] P. Shvets, O. Dikaya, K. Maksimova, A. Goikhman, *J. Raman Spectrosc.* **2019**, 50, 1226.
- [23] A. C. Ferrari, *Solid State Commun.* **2007**, 143, 47.
- [24] R. A. Cox, Ü. L. Haldna, K. L. Idler, K. Yates, *Can. J. Chem.* **1981**, 59, 2591.
- [25] K. Tomikawa, H. Kanno, *J. Phys. Chem. A* **1998**, 102, 6082.
- [26] O. R. Hunt, A. D. Ward, M. D. King, *RSC Adv.* **2013**, 3, 19448.
- [27] G. T. Strandford, R. A. Condrate, *J. Solid State Chem.* **1985**, 56, 394.
- [28] Z. Jiang, K. Klyukin, V. Alexandrov, *J. Chem. Phys.* **2016**, 145, 114303.
- [29] N. Kausar, R. Howe, M. Skyllas-Kazacos, *J. Appl. Electrochem.* **2001**, 31, 1327.
- [30] K. Kanamori, Y. Ookubo, K. Ino, K. Kawai, H. Michibata, *Inorg. Chem.* **1991**, 30, 3832.
- [31] M. B. Smirnov, E. M. Roginskii, K. S. Smirnov, R. Baddour-Hadjean, J.-P. Pereira-Ramos, *Inorg. Chem.* **2018**, 57, 9190.
- [32] F. Ureña-Begara, A. Crunteanu, J.-P. Raskin, *Appl. Surf. Sci.* **2017**, 403, 717.
- [33] C. Madic, G. M. Begun, R. L. Hahn, J. P. Launay, W. E. Thiessen, *Inorg. Chem.* **1984**, 23, 469.
- [34] C. Sun, K. Vezzù, G. Pagot, A. Nale, Y. H. Bang, G. Pace, E. Negro, C. Gambaro, L. Meda, T. A. Zawodzinski, V. Di Noto, *Electrochim. Acta* **2019**, 318, 913.
- [35] H. Radinger, V. Trouillet, F. Bauer, F. Scheiba, *ACS Catal.* **2022**, 12, 6007.
- [36] J. Kim, N. Lee, Y. H. Min, S. Noh, N.-K. Kim, S. Jung, M. Joo, Y. Yamada, *ACS Omega* **2018**, 3, 17789.
- [37] M. A. Pimenta, G. Dresselhaus, M. S. Dresselhaus, L. G. Cançado, A. Jorio, R. Saito, *Phys. Chem. Chem. Phys.* **2007**, 9, 1276.
- [38] V. Di Noto, G. Pagot, E. Negro, K. Vezzù, P. J. Kulesza, I. A. Rutkowska, G. Pace, *Curr. Opin. Electrochem.* **2022**, 31, 100839.
- [39] R. Baddour-Hadjean, M. B. Smirnov, K. S. Smirnov, V. Y. Kazimirov, J. M. Gallardo-Amores, U. Amador, M. E. Arroyo-de Domípablo, J. P. Pereira-Ramos, *Inorg. Chem.* **2012**, 51, 3194.
- [40] Z. Bo, S. Qing, H. De-Yan, *Chin. Phys. B* **2009**, 18, 4988.
- [41] R. Baddour-Hadjean, M. B. Smirnov, V. Y. Kazimirov, K. S. Smirnov, J.-P. Pereira-Ramos, *J. Raman Spectrosc.* **2015**, 46, 406.

- [42] Q. Hao, S. M. Morton, B. Wang, Y. Zhao, L. Jensen, T. Jun Huang, *Appl. Phys. Lett.* **2013**, *102*, 11102.
- [43] S. Lee, M. Kim, S.-Y. Cho, D.-J. Lee, H.-M. Kim, K.-B. Kim, *Nanotechnology* **2020**, *31*, 95708.
- [44] S. S. Nanda, M. J. Kim, K. S. Yeom, S. S. A. An, H. Ju, D. K. Yi, *TrAC Trends Anal. Chem.* **2016**, *80*, 125.
- [45] M. Inaba, H. Yoshida, Z. Ogumi, T. Abe, Y. Mizutani, M. Asano, *J. Electrochem. Soc.* **1995**, *142*, 20.
- [46] V. A. Sethuraman, L. J. Hardwick, V. Srinivasan, R. Kostecki, *J. Power Sources* **2010**, *195*, 3655.
- [47] S. Jovanovic, P. Jakes, S. Merz, R.-A. Eichel, J. Granwehr, *Electrochem. Sci. Adv.* **2021**, *2*, e2100068.
- [48] A. Moissette, A. Burneau, J. Dubessy, H. Fuzellier, M. Lelaurain, *Carbon* **1995**, *33*, 1223.
- [49] Y. Lin, Q. Lu, F. Song, L. Yu, A. K. Mechler, R. Schlögl, S. Heumann, *Angew. Chem. Int. Ed.* **2019**, *58*, 8917.

Manuscript received: October 1, 2022
Revised manuscript received: December 8, 2022
Accepted manuscript online: December 13, 2022
Version of record online: January 3, 2023